Materials Advances

Accepted Manuscript

This article can be cited before page numbers have been issued, to do this please use: S. Hegazy, N. Byrne, A. Abdelrahim, T. Hu, V. Srivastava, S. Tuomikoski and L. Ulla, *Mater. Adv.*, 2026, DOI: 10.1039/D6MA00412A.

ROYAL SOCIETY OF CHEMISTRY

rsc.li/materials-advances

View Article Online
DOI: 10.1039/D6MA00412A

Improving initial coulombic efficiency of wood-waste hard carbon: key factors controlling first-cycle irreversibility and practical mitigation strategies

Sherif Hegazy[a], Nolene Byrne[b], Ahmed Abdelrahim[c], Tao Hu[a], Varsha Srivastava[a], Sari Tuomikoski[a], Ulla Lassi[a]

[a] Research Unit of Sustainable Chemistry, University of Oulu, P.O. Box 4300, FI-90014 Oulu, Finland.

[b] Institute for Frontier Materials, Deakin University, Burwood, Victoria 3125, Australia.

[c] Process Metallurgy Research Unit, University of Oulu, Pentti Kaiteran katu 1, FI-90014 Oulu, Finland.

*Corresponding author: Prof. Ulla Lassi (Email: Ulla.Lassi@oulu.fi)

Abstract

Low initial coulombic efficiency (ICE) remains a major barrier for biomass-derived hard carbon anodes in sodium-ion batteries (SIBs), where first-cycle Na loss is dominated by interphase formation and irreversible trapping. Here, we improve and rationalize ICE in wood-waste (WW)-derived hard carbon by combining intrinsic and extrinsic strategies within one framework. Intrinsically, metal organic framework (MOF)-assisted catalytic processing increases local structural order, raising ICE from 26% (WW) to 41% with a first-charge capacity of 191 mAh g^{-1}. Extrinsically, the catalyst-treated carbon is evaluated in carbonate and ionic-liquid electrolytes, including a low-salt NaFSI–EMIFSI (10 mol% NaFSI) benchmark and NaFSI–C_3MPYRFSI (50:50 mol%). While $NaPF_6$–EC/PC delivers a slightly higher ICE (42%), the ionic-liquid electrolytes provide higher reversible capacities (up to 195 mAh g^{-1}) and improved retention. Finally, direct-contact pre-sodiation increases ICE to 75% at an optimized contact time of 15 min (approximately threefold higher than the untreated WW carbon), whereas longer contact lowers reversible capacity. Impedance analysis and rate/cycling tests confirm improved interfacial kinetics and stability. Overall, this combined approach mitigates first-cycle losses and places the ICE improvement among the larger gains reported for biomass-derived hard carbons.

View Article Online
DOI: 10.1039/D6MA00412A

Keywords:

Catalytic graphitization, Initial coulombic efficiency, Ionic liquid electrolyte, Pre-sodiation, Sodium-ion batteries

1. Introduction

The rapid growth of renewable electricity generation and electrified transportation is accelerating demand for cost-effective and sustainable electrochemical energy storage.[1] Sodium-ion batteries (SIBs) are widely viewed as a significant alternative to lithium-ion technology for large-scale applications because sodium resources are abundant and broadly distributed.[2] Within SIB chemistries, hard carbon (HC) has emerged as the most practical anode candidate due to its low operating potential, good cycling stability, and compatibility with scalable synthesis from diverse precursors, especially biomass.[3]

Hard carbon is commonly classified as a non-graphitizable form of carbon. Structurally, it consists of small, graphitic-like domains that are irregularly oriented and separated by disordered/amorphous carbon, forming a rigid, turbostratic framework. In contrast to soft (graphitizable) carbon, this arrangement does not readily transform into long-range, well-aligned graphite, even under very high heat-treatment temperatures (often exceeding 2500 °C).[4] HC is typically obtained by pyrolyzing biomass or synthetic organic precursors, and many morphological features such as porosity, particle

View Article Online
DOI: 10.1039/D6MA00412A

shape, and texture are partly retained from the original feedstock, making precursor selection and thermal history key parameters for controlling microstructure and electrochemical behavior.[5,6]

Despite its advantages, the main limitation of HC in practical SIB full cells is its low initial coulombic efficiency (ICE).[7] ICE reflects how much of the sodium inserted during the first sodiation can be recovered in the first de-sodiation, and it therefore determines how much cyclable sodium is consumed during cell formation. For HC anodes, the first-cycle loss is mainly associated with two irreversible processes: (i) electrolyte decomposition and SEI formation on reactive carbon surfaces and within accessible pores, and (ii) irreversible Na trapping at high-energy sites such as defects/edges, heteroatom-related sites, and in certain micropore environments.[4,8,9] Consequently, improving ICE requires enhancing reversible Na storage, while reducing side reactions and avoiding Na trapping so that the inserted sodium can be extracted again.[10,11]

ICE-improvement approaches are typically grouped into two categories. Intrinsic strategies focus on the carbon material itself by adjusting features such as defect concentration, structural order, interlayer characteristics, and pore structure through choices in precursor, heat-treatment conditions, and structural modification methods (e.g., templating, surface coating, or catalytic treatments during carbonization).[12,13] Beyond hard carbon, structural and interface engineering of other carbon-based anode systems — including dual-carbon confinement strategies and composite architectures — has similarly demonstrated that controlling carbon microstructure and interfacial chemistry are critical for improving cycling stability and first-cycle performance in SIBs.[14–16]

Extrinsic strategies act outside the carbon framework by regulating how the interphase forms—most commonly through electrolyte selection/additives—or by offsetting unavoidable first-cycle sodium losses using pre-sodiation. In practice, improving biomass-derived hard carbon in a full-cell-relevant way often requires combining these directions: tailoring the carbon microstructure while simultaneously controlling interphase chemistry and managing the available sodium inventory.[17]

View Article Online
DOI: 10.1039/D6MA00412A

In this work, we address ICE limitations in wood-waste-derived hard carbon by combining intrinsic and extrinsic strategies within one framework. On the intrinsic side, the carbon microstructure is tuned using MOF-assisted catalytic treatments, and the effect of catalyst chemistry is assessed by comparing Fe-MOF, Zr-MOF, and Fe–Zr-MOF routes with ICE as the key metric. For the extrinsic part, we test the top-performing carbon under different interphase conditions using both carbonate and ionic-liquid electrolytes. In addition, we apply pre-sodiation as a controlled step to compensate irreversible sodium consumption. By combining these strategies, we aim to clarify the factors governing first-cycle irreversibility and provide practical routes to improve ICE while maintaining competitive capacity and cycling stability.

2. Experimental

2.1. Materials

Waste Wood (WW) derived carbon (pyrolyzed at 650 °C for 1 h) was provided by Karelian Paju Company (Finland). All reagents were analytical grade and were used as received, without additional purification. Iron (III) chloride ($FeCl_3$, >98%), hydrochloric acid (HCl), and sodium hydroxide (NaOH) were purchased from Merck (Germany). Anhydrous zirconium (IV) chloride ($ZrCl_4$, 99.99%), sodium metal, and carbon black were obtained from Sigma-Aldrich. 2-Aminoterephthalic acid ($C_8H_7NO_4$, >98%) was supplied by TCI (Japan). N, N-dimethylformamide (DMF, >98%), acetonitrile (ACN, max. 0.001% water), and absolute ethanol were purchased from VWR (UK). Battery-grade sodium bis(fluorosulfonyl)imide (NaFSI, 99.7%) and N-propyl-N-methylpyrrolidinium bis(fluorosulfonyl)imide (C3mpyrFSI, 99.9%) were obtained from Solvionic Corporation.

View Article Online
DOI: 10.1039/D6MA00412A

2.2. Experimental Methods

WW@FeMOF. 2-Aminoterephthalic acid (0.56 g) was dissolved in DMF (15 mL). In parallel, wood-waste carbon (10 g) was dispersed in DMF (25 mL) in a 250 mL screw-cap bottle and stirred for 20 min. Separately, $FeCl_3$ (0.605 g) was dissolved in DMF (24.05 mL) and then added to the carbon/ligand suspension under stirring.

WW@ZrMOF. The same procedure was followed using 2-aminoterephthalic acid (0.431 g) dissolved in DMF (31.71 mL), with wood-waste carbon (10 g) dispersed in DMF (25 mL). $ZrCl_4$ (0.605 g) was dissolved in DMF (20 mL) and subsequently added to the carbon/ligand mixture.

WW@Fe–ZrMOF. The bimetallic sample was synthesized using the identical protocol, while introducing *both* metal precursors at the same amounts used in the monometallic syntheses ($FeCl_3$, 0.605 g and $ZrCl_4$, 0.605 g) together with the corresponding ligand solutions described above, followed by mixing with the carbon dispersion.

For all syntheses, the bottle was sealed and the reaction mixture was stirred at 80 °C for 12 h. The solids were collected by filtration, washed with acetonitrile (ACN), and solvent-exchanged using preheated ACN at 80 °C for 2 h under autogenous pressure. Finally, the products were filtered and dried at 80 °C. This protocol was adapted from our previous work where successful MOF crystallization on the carbon surface was confirmed by XRD and FTIR.[18,19] The dried samples were pyrolyzed under argon flow (2 L min^{-1}) following a stepwise temperature program: heating from room temperature to 900 °C at a ramp rate of 5 °C min^{-1}, holding at 900 °C for 4 h, and then allowing the furnace to naturally cool to room temperature. After pyrolysis, the samples were acid-washed to remove metal compounds by stirring the carbon in an HCl (37%): HNO_3 (69%): H_2O (1:1:2, v/v/v) solution (40 mL g^{-1}) at 120 °C for 3 h, followed by filtration. The acid-washing leachates were analysed by inductively coupled plasma optical emission spectroscopy (ICP-OES) to quantify dissolved metal species; the measured concentrations are summarized in **Table S3**.

2.3. Characterization

View Article Online
DOI: 10.1039/D6MA00412A

All materials were characterized at the University of Oulu (Finland). The detailed instrument models and operating parameters are summarized in the Supplementary Information (SI).

2.4. Electrode preparation and electrochemical measurements

Working electrodes were prepared by mixing the active material, conductive carbon (Super C65), and PVDF binder in a weight ratio of 8:1:1. N-methyl-2-pyrrolidone (NMP) was used as the solvent to form a homogeneous slurry, which was cast onto aluminium foil using a 50 µm doctor blade. The coated electrodes were dried under vacuum at 120 °C overnight, then punched into 14 mm diameter discs. The active material loading was approximately 2.0 ± 0.2 mg cm^{-2}.

CR2032 half-cells were assembled in an argon-filled glovebox (MBraun), with O_2 and H_2O levels maintained below 0.1 ppm. The prepared electrodes served as the working electrodes, while sodium metal discs (12 mm diameter) were used as both counter and reference electrodes. A Solupor® separator (14 mm diameter) was placed between the electrodes, and 60 µL of electrolyte was added to each cell.

Three electrolytes were evaluated: (i) an ionic liquid electrolyte prepared by mixing NaFSI and EMIFSI at a 10% molar ratio, (ii) an ionic liquid electrolyte based on NaFSI and C_3mpyrFSI mixed at a 50:50 mol%, and (iii) a carbonate-based electrolyte consisting of 1 M $NaPF_6$ in EC: PC (1:1 by volume).

For pre-sodiation, a thin sodium metal layer was placed directly on the electrode with 30 µL of electrolyte to ensure ionic contact. The assembly was then gently pressed under a constant load (60 g) to maintain uniform interfacial contact, and the contact time was controlled at 10, 15, 20, or 30 min before cell assembly. After the contact period, the sodium metal layer was removed, and the electrode was directly used for cell assembly without rinsing.

Prior to testing, assembled cells were rested for 24 h to ensure complete wetting: at 25 °C for carbonate-based cells and at 50 °C for ionic liquid-based cells. Galvanostatic cycling was performed using a BioLogic BCS-810 system within a voltage window of 0.01–2.0 V vs. Na^+/Na. Each cell was

View Article Online
DOI: 10.1039/D6MA00412A

subjected to five formation cycles at C/10, followed by prolonged cycling at C/5. The C-rate was defined based on a nominal hard-carbon capacity of 250 mAh g^{-1}, corresponding to current densities of 25 mA g^{-1} (C/10), 50 mA g^{-1} (C/5), 125 mA g^{-1} (C/2), 250 mA g^{-1} (1C), and 500 mA g^{-1} (2C). Rate capability was evaluated by cycling at C/10, C/5, C/2, 1C, and 2C for five cycles at each current, followed by repeating the same sequence. Cyclic voltammetry (CV) was conducted on a BioLogic VSP potentiostat at a scan rate of 0.1 mV s^{-1} for five cycles. Electrochemical impedance spectroscopy (EIS) measurements were recorded at open-circuit voltage using a 10 mV AC perturbation over a frequency range of 10^5 to 10^{-1} Hz.

3. Results and Discussion

3.1. Material characteristics:

The structure of the wood-waste hard carbons was examined by XRD, Raman spectroscopy, and XPS. In hard carbon, sodium storage is strongly influenced by the coexistence of disordered carbon and short graphitic-like stacks, as well as by the interlayer spacing (d_{002}), which is inherited from the precursor and modified by processing conditions.[20,21]

The XRD patterns (**Fig. 1a**) show two broad carbon-related features centered at ~29° and ~49° (2θ). These can be assigned to the (002) and (101) reflections of hexagonal graphite (ICDD: 01-074-2329). Their weak and broadened appearance indicates limited stacking order and turbostratic character, consistent with a hard-carbon framework. Importantly, the position of the (002) feature shifts depending on the catalyst route, leading to measurable differences in (d_{002}) (**Table S1**). WW@FeMOF exhibits the smallest interlayer distance (3.46 Å) compared with WW (3.50 Å), whereas WW@ZrMOF shows an expanded spacing (3.58 Å), WW@Fe–ZrMOF falls between these

View Article Online
DOI: 10.1039/D6MA00412A

values (3.54 Å). All spacings are larger than that of crystalline graphite (3.35 Å), which is generally considered beneficial for Na^+ insertion because the larger ion can be accommodated more readily between the carbon layers.[22] In addition to the carbon features, the Zr-containing samples show sharp reflections at ~35°, 41°, 59°, and 71° (2θ), consistent with residual crystalline ZrO_2 (ICDD: 04-005-9740). Raman spectra (**Fig. 1b**) display the characteristic D (~1340 cm^{-1}) and G (~1580 cm^{-1}) bands of hard carbon. The pristine WW shows the highest disorder ($I_D/I_G = 1.28$), while MOF-assisted treatment lowers I_D/I_G, reaching 0.77 for WW@FeMOF (and WW@Fe–ZrMOF) and 0.93 for WW@ZrMOF. The reduced I_D/I_G indicates fewer defect-related sites and increased structural ordering. This trend agrees with the expected role of catalytic species in promoting local ordering, as discussed in our previous work.[23] XPS was used to examine the surface chemistry of WW@FeMOF, confirming that the surface is mainly composed of carbon and oxygen; this sample was selected for XPS as the best-performing electrode. The high-resolution C 1s spectrum (**Fig. 1c**) can be fitted with four components at 284.8, 286.0, 287.2, and 288.7 eV, assigned to C–C, C–O, C=O, and O–C=O, respectively. Corresponding oxygen functionalities are also observed in the O 1s spectrum (**Fig. 1d**), with contributions at 533.6 eV (C–O), 531.2 eV (C=O), and 532.4 eV (O–C=O) [74]. The same functional groups are present in the untreated WW sample (**Fig. S1**); however, MOF-assisted processing slightly increases the atomic contribution of the C–C component from 56.7% to 58.0% (**Table S2**), consistent with a modest shift toward a more carbon-rich surface.

View Article Online
DOI: 10.1039/D6MA00412A

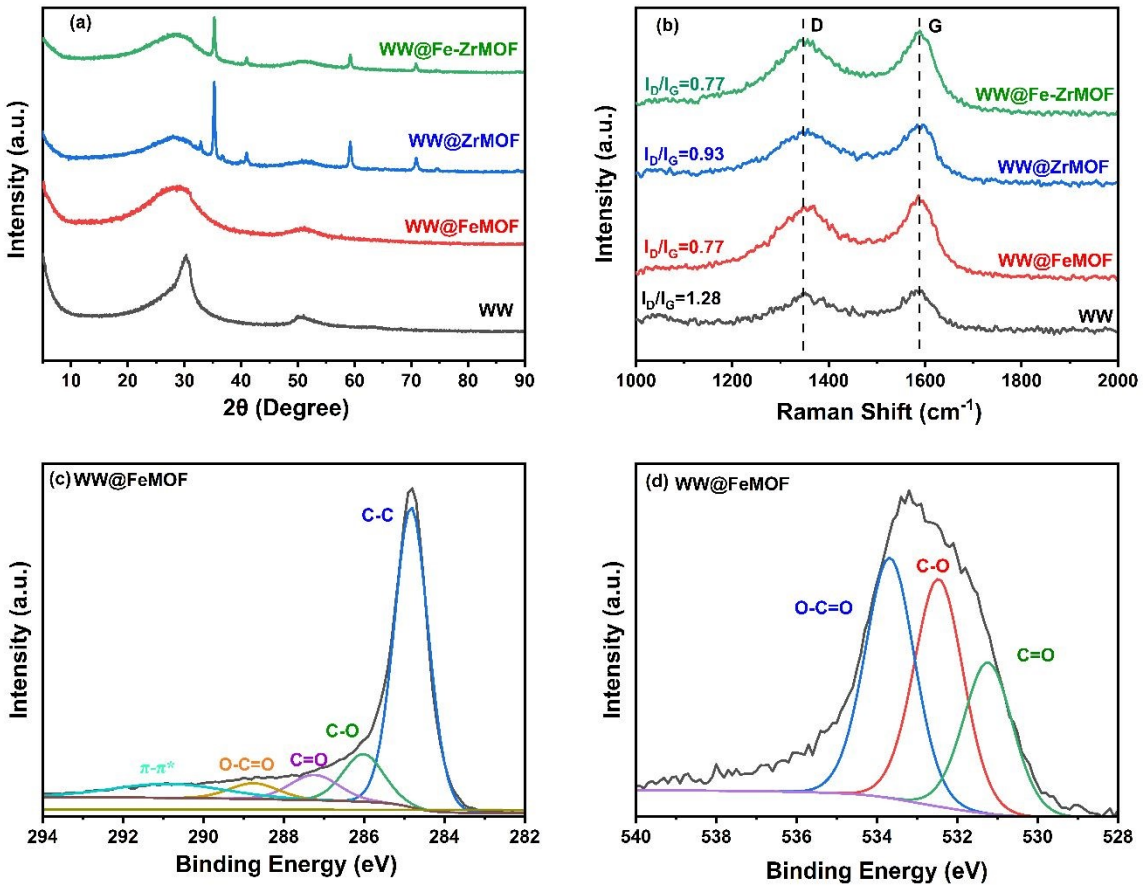

Fig.1. (a) XRD patterns and (b) Raman spectra of WW, WW@FeMOF, WW@ZrMOF, and WW@Fe–ZrMOF. (c) High-resolution C 1s and (d) O 1s XPS spectra of WW@FeMOF with peak deconvolution.

The textural properties derived from N_2 sorption analysis are summarized in **Table 1**. The pristine WW sample shows the highest specific surface area (393 m^2 g^{-1}) and total pore volume (0.19 cm^3

View Article Online
DOI: 10.1039/D6MA00412A

g^{-1}), with a notable mesopore contribution (29%). After MOF-assisted processing, the surface area decreases to 280–323 $m^2\ g^{-1}$ and the pore volume drops to 0.12–0.14 $cm^3\ g^{-1}$, accompanied by a shift toward a predominantly microporous structure. Specifically, the micropore fraction increases from 70% (WW) to ~82.5–83.5% for the MOF-derived samples, while the mesopore fraction decreases to ~15.5–16.5%. In addition, the average pore diameter narrows from 2.1 nm (WW) to ~1.8 nm for the MOF-treated carbons. Among the catalyzed samples, WW@FeMOF and WW@ZrMOF exhibit very similar textural parameters. N_2 adsorption–desorption isotherms for all samples are provided in the Supporting Information (**Fig. S2**). Elemental composition (**Table 2**) shows that all carbons are predominantly carbon-rich (76.4–83.1%), with oxygen as the main heteroatom (9.1–11.1%). Compared with WW (C = 83.11%, O = 9.12%, O/C = 0.11), MOF-assisted samples display a higher oxygen content and higher O/C ratio, most notably for WW@ZrMOF (O = 11.13%, O/C = 0.14). The Fe-containing samples remain closer to the baseline in O/C (WW@FeMOF: 0.12; WW@Fe–ZrMOF: 0.11). Nitrogen is present only in small amounts (≤0.37%), while sulfur is not detected.

Table 1: Textural properties of WW, WW@FeMOF, WW@ZrMOF, and WW@Fe-ZrMOF samples.

Sample	Surface area ($m^2\ g^{-1}$)	Pore diameter (nm)	Pore Volume ($cm^3\ g^{-1}$)	Micro pores %	Meso pores %	Macro pores %
WW	393	2.1	0.19	70.0	29.0	1.0
WW@FeMOF	322	1.8	0.14	82.5	16.5	1.0
WW@ZrMOF	323	1.8	0.14	83.5	15.5	1.0
WW@Fe-ZrMOF	280	1.8	0.12	82.5	16.4	1.0

Table 2: Elemental composition (CHNSO, in wt.%) of WW, WW@FeMOF, WW@ZrMOF, and WW@Fe-ZrMOF samples.

View Article Online
DOI: 10.1039/D6MA00412A

Sample	Carbon (%)	Oxygen (%)	Hydrogen (%)	Nitrogen (%)	Sulfur (%)	O/C
WW	83.11	9.12	0.60	0.23	0	0.11
WW@FeMOF	80.14	10.11	0.73	0.34	0	0.12
WW@ZrMOF	76.40	11.13	0.69	0.37	0	0.14
WW@Fe-ZrMOF	80.80	9.14	0.63	0.35	0	0.11

HRTEM was used to examine how the MOF-assisted route changes the local carbon arrangement. The untreated WW sample (**Fig. 2a**) is mainly composed of disordered carbon, with no extended stacked-layer regions. After Fe-MOF treatment, WW@FeMOF (**Fig. 2b**) shows stacked carbon layers within the particle, coexisting with disordered regions. In the most ordered zones, the layered domains extend over several nanometres and contain tens of stacked graphene layers, indicating a clear increase in local graphitic ordering compared with WW.

The formation of these stacked-layer domains is consistent with the catalytic role of Fe-derived species generated during pyrolysis. Metallic Fe and iron carbide can promote carbon reorganization through a dissolution–precipitation process, as discussed in our previous work.[24]

SEM images (**Fig. 2c, d**) indicate that both samples retain the irregular, fractured morphology typical of wood-derived carbons. Compared with WW, WW@FeMOF exhibits a rougher surface with a higher fraction of fine fragments distributed between larger particles, suggesting that the MOF assisted treatment affects microstructural development while preserving the overall particle shape. The contrasting structural outcomes of the different MOF treatments can be rationalized by the catalytic behavior of the metal species formed during pyrolysis. Fe-derived species (Fe^0 and Fe_3C,) are well-established catalytic graphitization agents that promote carbon layer ordering through a dissolution–precipitation mechanism, accounting for the reduced d_{002} (3.46 Å) and lower I_D/I_G (0.77) in WW@FeMOF. In contrast, Zr forms refractory ZrO_2 during pyrolysis, which does not participate in graphitization; residual ZrO_2 at grain boundaries likely hinders layer reorganization, resulting in

View Article Online
DOI: 10.1039/D6MA00412A

higher disorder (I_D/I_G = 0.93) and expanded d_{002} (3.58 Å) in WW@ZrMOF. For the bimetallic WW@Fe–ZrMOF, the absence of synergistic improvement suggests that ZrO_2 partially suppresses Fe catalytic activity, possibly through competitive interactions that reduce the availability of active Fe^0 and Fe_3C phases during pyrolysis.

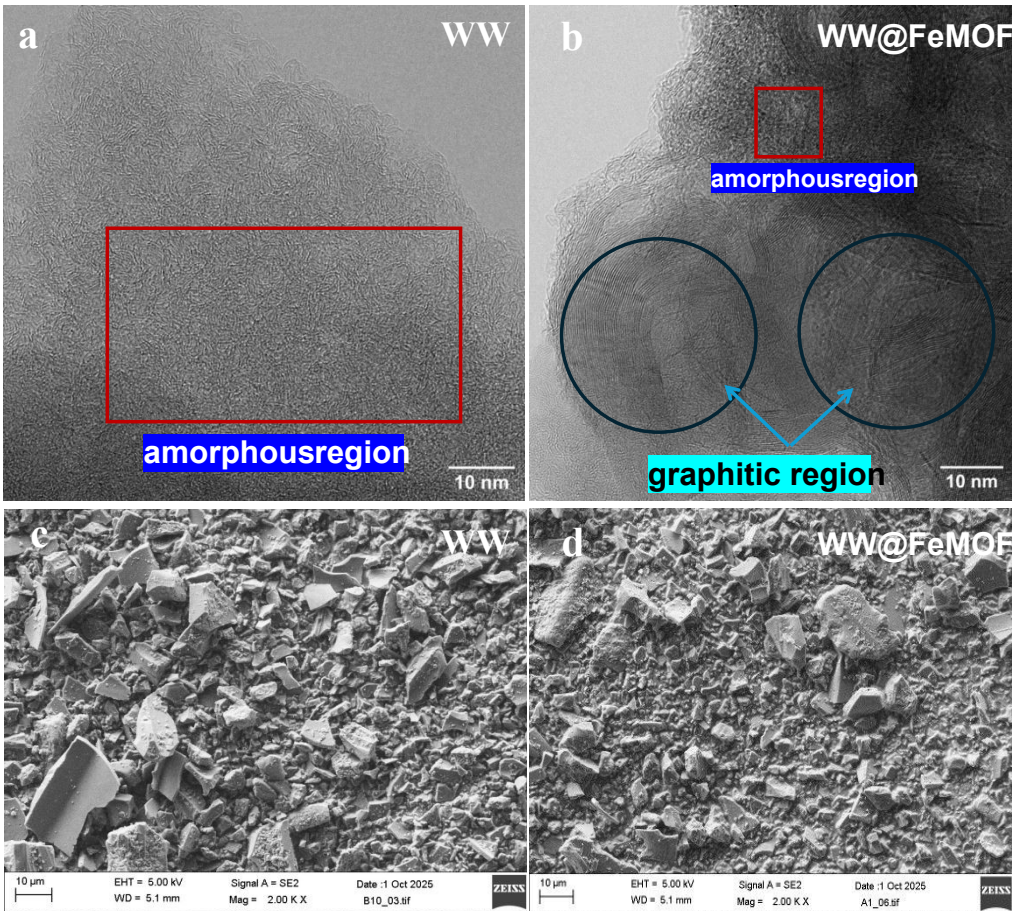

Fig. 2. (a,b) HRTEM images of WW and WW@FeMOF highlighting disordered carbon and stacked graphene-layer domains. (c,d) SEM images of WW and WW@FeMOF showing particle morphology.

3.2. **Electrochemical performance**

View Article Online
DOI: 10.1039/D6MA00412A

3.2.1. **Effect of catalyst type on ICE%**

The first cycle charge–discharge response of WW and the MOF-treated carbons was evaluated in Na half-cells using 10 mol% NaFSI–EMIFSI electrolyte (**Fig. 3**). The catalyst chemistry has a strong impact on the (ICE). The untreated WW delivers an ICE of 26% with a charge capacity of 118 mAh g^{-1}. Among the catalyzed samples, WW@FeMOF shows the best performance, reaching an ICE of 41% together with the highest charge capacity (191 mAh g^{-1}). In contrast, WW@ZrMOF exhibits the lowest ICE (22%) and a lower capacity (94 mAh g^{-1}), while WW@Fe–ZrMOF gives intermediate results (ICE 37.5%, 148 mAh g^{-1}). The lower ICE of WW@ZrMOF is consistent with its lower carbon content and higher O/C ratio (**Table 2**), which increases electrolyte decomposition sites during the first cycle and likely contributes to greater irreversible sodium loss.[25] Residual crystalline ZrO_2 detected by XRD may further increase first-cycle losses by adding electrochemically inactive interfaces.

To further correlate structural changes with sodium storage behavior, the sloping and plateau capacity contributions were extracted from the 2nd cycle profiles (**Fig. 3e, f**). WW@FeMOF exhibits the highest plateau capacity (50 mAh g^{-1}, ~27% of total discharge capacity), consistent with its smallest interlayer spacing (d_{002} = 3.46 Å) and highest structural order (I_D/I_G = 0.77), which together facilitate reversible Na^+ insertion between more organized carbon layers. Notably, WW@ZrMOF shows a plateau contribution (26 mAh g^{-1}) comparable to the untreated WW (25 mAh g^{-1}), despite having the largest d_{002} (3.58 Å), indicating that expanded interlayer spacing alone is insufficient to improve plateau storage when structural disorder remains high and residual ZrO_2 is present, consistent with the low ICE observed for this sample. WW@Fe–ZrMOF shows an intermediate plateau capacity (47 mAh g^{-1}), broadly consistent with its intermediate structural order (I_D/I_G = 0.77, d_{002} = 3.54 Å). Overall, the plateau capacity trend follows the degree of structural ordering rather than interlayer spacing alone, with WW@FeMOF offering the most favorable combination of both parameters.

View Article Online
DOI: 10.1039/D6MA00412A

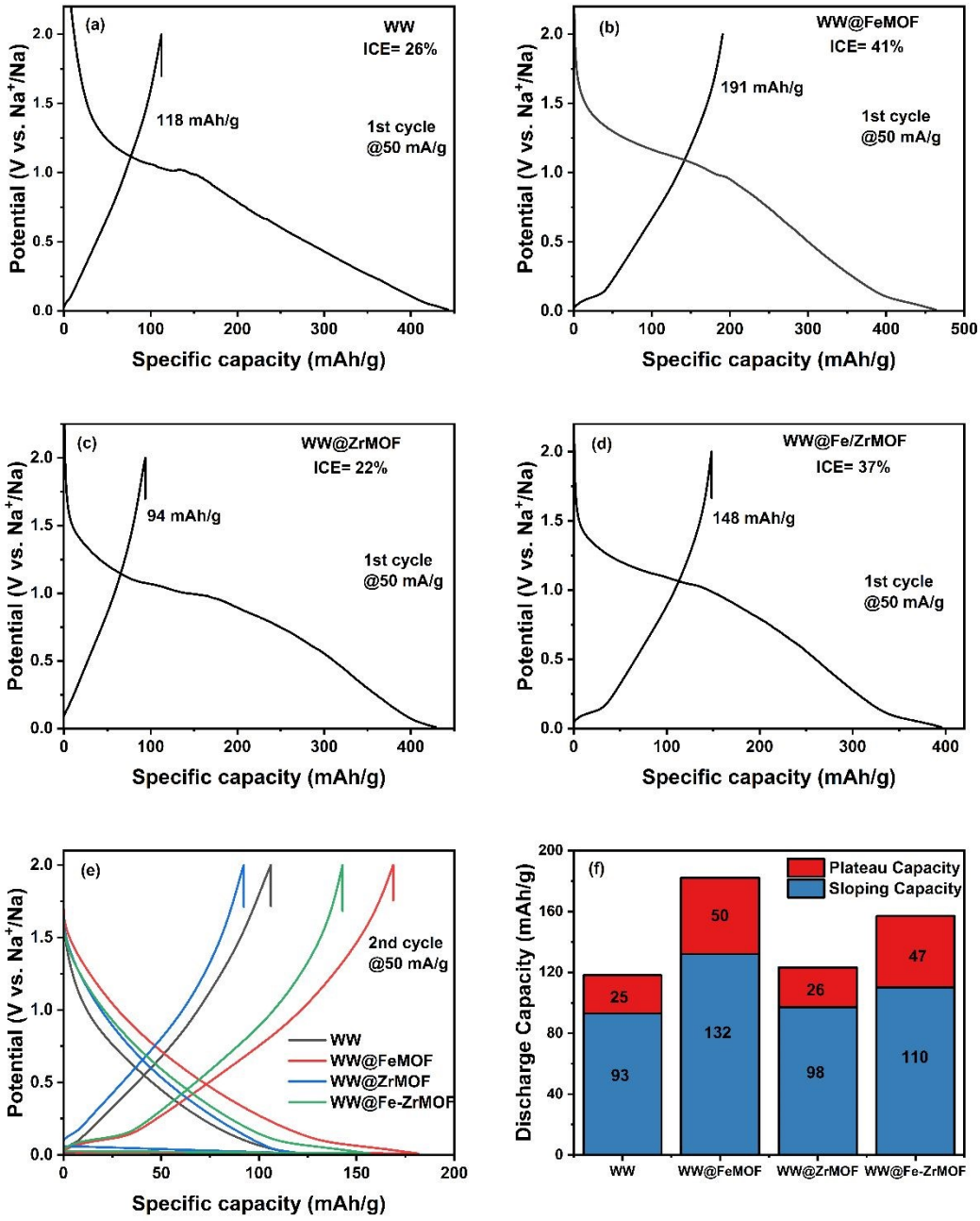

Fig. 3. First-cycle charge–discharge profiles of (a) WW, (b) WW@FeMOF, (c) WW@ZrMOF, (d) WW@Fe–ZrMOF in Na half-cells with 10 mol% NaFSI–EMIFSI electrolyte, (e) 2nd cycle charge–discharge profiles of all samples, and (f) Sloping and plateau capacity contributions extracted from the 2nd cycle profiles.

3.2.2 Effect of electrolyte type on ICE%

View Article Online
DOI: 10.1039/D6MA00412A

The influence of electrolyte chemistry on the first-cycle behavior and cycling stability of WW@FeMOF was examined using two ionic-liquid electrolytes NaFSI–EMIFSI (1:9) and NaFSI–C_3MPYRFSI (1:1; 50:50 mol%) and a carbonate electrolyte (1 M $NaPF_6$ in EC/PC) (**Fig.4**). The carbonate electrolyte gives a slightly higher ICE (42%) than the ionic-liquid systems (40% for NaFSI–EMIFSI and 40.6% for NaFSI–C_3MPYRFSI). The reversible capacity, however, is clearly higher in the ionic-liquid electrolytes: the first-charge capacities reach 188–195 mAh g^{-1}, compared with 130 mAh g^{-1} in EC/PC (**Fig. 4a–c**). This difference carries into cycling (**Fig. 4d**), where the ionic-liquid electrolytes maintain higher capacities over the tested range. The small ICE differences likely reflect electrolyte-dependent interphase formation. Carbonate electrolytes (EC/PC) often form carbonate-rich SEI products that passivate the surface early, which can slightly improve ICE.[26,27] In FSI-based ionic liquids, interphase formation is more strongly influenced by anion-derived reactions and salt coordination, which can change charge-transfer kinetics and capacity utilization, particularly at higher NaFSI fractions.[28–30] This provides a reasonable framework for comparing the low-salt NaFSI–EMIFSI electrolyte (10 mol% NaFSI) with NaFSI–C_3MPYRFSI formulation containing 50 mol% NaFSI, where the higher salt fraction is expected to bias interphase formation more strongly toward FSI-derived species. Low-salt imidazolium-based IL formulations have been previously reported for sodium battery systems, with 0.1 NaTFSI–0.9 EMIFSI demonstrating a room temperature ionic conductivity of 8.6×10^{-3} S cm^{-1}, confirming the ionic transport suitability of low-salt EMIFSI electrolytes for sodium battery applications.[31,32]

Impedance measurements recorded after formation support this trend. As shown in (**Fig. 4e)**, both ionic-liquid electrolytes exhibit lower overall impedance than $NaPF_6$–EC/PC, and the resistance values extracted from these spectra (**Fig. 4f**) indicate a much higher charge-transfer resistance in the carbonate electrolyte. This higher interfacial resistance matches the lower capacity and weaker retention in EC/PC. In contrast, the ionic-liquid electrolytes show lower impedance and better

capacity retention, indicating a more favourable electrode–electrolyte interface for Na insertion/extraction despite similar ICE values.

View Article Online
DOI: 10.1039/D6MA00412A

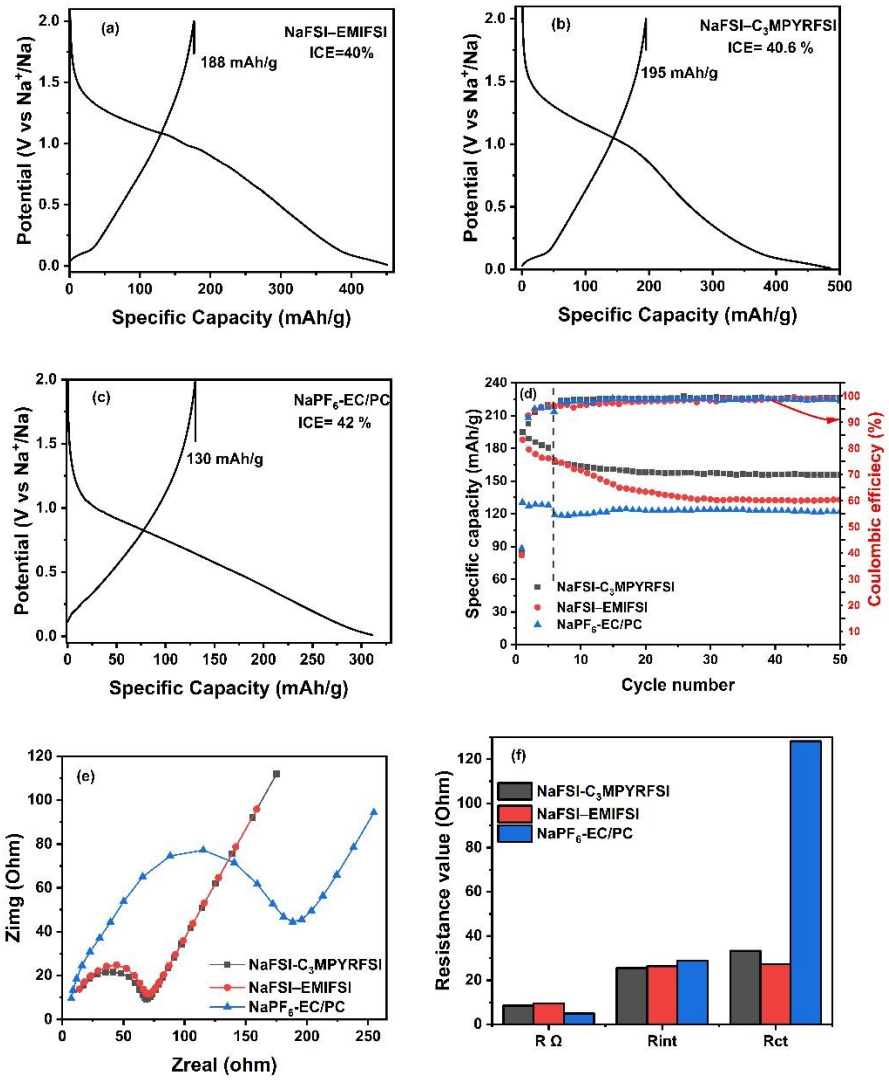

Fig. 4. (a–c) First-cycle charge–discharge profiles of WW@FeMOF in Na half-cells using (a) NaFSI–EMIFSI (10 mol% NaFSI), (b) NaFSI–C_3MPYRFSI (50:50 mol%), and (c) 1 M $NaPF_6$ in EC/PC (1:1, v/v). (d) Cycling performance of WW@FeMOF in the three electrolytes. (e) Nyquist plots measured after the 5th cycle. (f) Resistance values (RΩ, Rint, Rct) extracted from the impedance spectra.

View Article Online
DOI: 10.1039/D6MA00412A

3.2.3. Effect of pre-sodiation on ICE%

The effect of direct-contact pre-sodiation on the first-cycle reversibility of WW@FeMOF was evaluated in Na half-cells using 10 mol% NaFSI–EMIFSI (**Fig. 5**). Compared with the non-presodiated electrode (ICE ~40%, discussed above), pre-sodiation increases ICE to 58% after 10 min (first-charge capacity 135 mAh g^{-1}) and reaches a maximum of 75% after 15 min with a high first-charge capacity (181 mAh g^{-1}). Longer contact times lead to a decline: at 20 min the ICE decreases to 62.2% (138 mAh g^{-1}), and at 30 min it drops to 52.4% (120 mAh g^{-1}). This non-monotonic trend is consistent with direct-contact pre-sodiation compensating irreversible Na loss and partially forming the interphase prior to cycling.[33] The decrease at longer contact times suggests over-presodiation, where excess Na uptake and/or a more developed passivation layer begins to limit accessible reversible storage sites. While sodium metal handling requires inert-atmosphere conditions, the direct-contact method has been described as a simple, fast, and cost-effective pre-sodiation approach with potential applicability in practical battery manufacturing. [33,34]

View Article Online
DOI: 10.1039/D6MA00412A

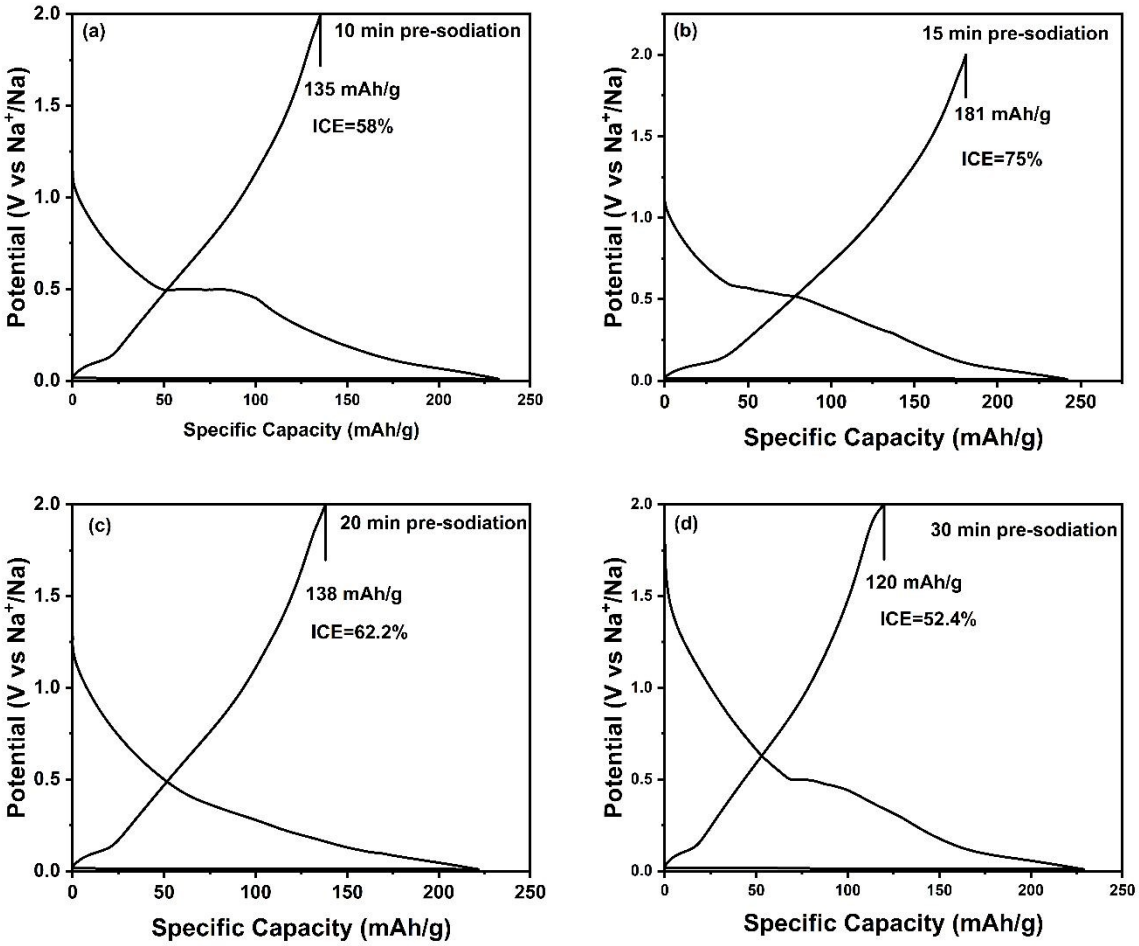

Fig. 5. First-cycle charge–discharge profiles of WW@FeMOF in Na half-cells with 10 mol% NaFSI–EMIFSI after direct-contact pre-sodiation for (a) 10 min, (b) 15 min, (c) 20 min, and (d) 30 min.

3.3. Kinetics, interfacial resistance, and cycling stability

To understand the Na-storage mechanism and the origin of the first irreversible loss, CV was recorded for WW@FeMOF and WW at 0.1 mV s^{-1} (**Fig. 6a, b**). In the first scan, both electrodes show a broad cathodic peak in the 0.6–1.0 V range, commonly assigned to electrolyte reduction and SEI formation; this feature largely disappears in subsequent cycles, indicating that most interphase formation occurs during the first cycle.[35] WW exhibits a stronger first-cycle cathodic response, consistent with more extensive irreversible reactions during formation.[36] In addition, WW@FeMOF shows a distinct low-

View Article Online
DOI: 10.1039/D6MA00412A

voltage reduction peak near ~0.02 V with a corresponding oxidation peak at ~0.1–0.2 V, which are typically associated with reversible low-potential Na storage/extraction in hard carbon.[37] The closer overlap of the 2nd and 5th scans for WW@FeMOF further indicates faster stabilization after formation. Nyquist plots measured after the formation cycles (**Fig. 6c**) show a clear reduction in impedance for WW@FeMOF compared with WW. The smaller semicircle indicates lower interfacial and charge-transfer resistances, consistent with improved kinetics and a more stable electrode–electrolyte interface; the fitted resistance values are summarized in **Fig. S3**.

This kinetic advantage is also reflected in the rate capability results (**Fig. 6d**). WW@FeMOF delivers higher capacities than WW across all applied current densities and shows better recovery when the current is returned to lower rates, pointing to lower polarization and more effective utilization of Na-storage sites.

Long-term cycling performance is shown in (**Fig. 6e, f**). WW@FeMOF maintains a substantially higher reversible capacity than WW over extended cycling, while the coulombic efficiency rapidly approaches ~100% after the formation period. Although WW also stabilizes in efficiency after the initial cycles, it operates at a consistently lower capacity. Overall, these results demonstrate that Fe-MOF treatment improves kinetics, reduces interfacial resistance, and enhances long-term cycling stability in the NaFSI–EMIFSI electrolyte.

View Article Online
DOI: 10.1039/D6MA00412A

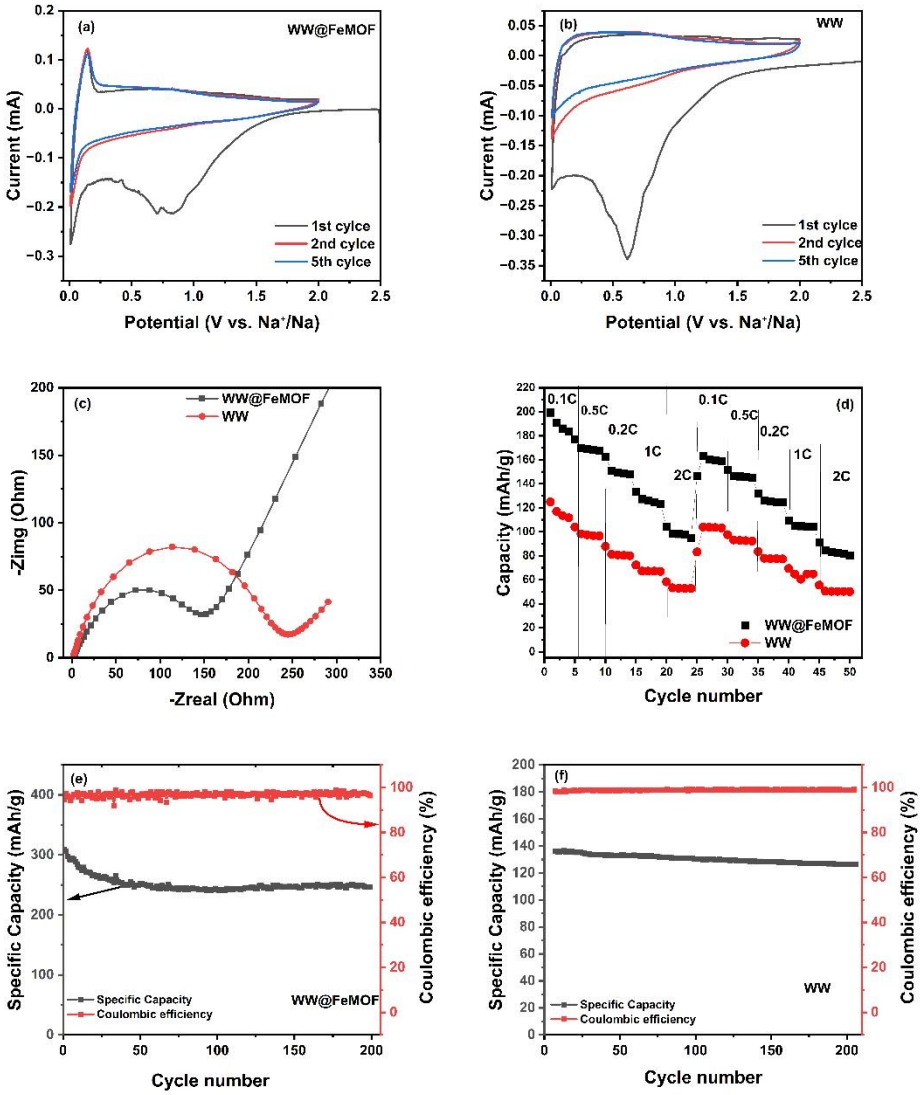

Fig. 6. Electrochemical comparison of WW@FeMOF and WW in Na half-cells using 10 mol% NaFSI–EMIFSI: (a,b) CV curves (1st, 2nd, and 5th cycles), (c) Nyquist plots measured after the 5th cycle with equivalent-circuit fitting, (d) rate capability, and (e,f) long-term cycling performance with coulombic efficiency.

Table 3 compares reported approaches used to raise ICE in hard-carbon anodes, including thermal optimization, surface modification, electrolyte tuning, and pre-sodiation. The achieved improvement varies widely with precursor and testing conditions. In this work, combining MOF-assisted

View Article Online
DOI: 10.1039/D6MA00412A

microstructure tuning with electrolyte selection and controlled pre-sodiation increased ICE from 26% to 75% (ΔICE = +49 pp), placing the result among the higher ICE gains reported for biomass-derived hard carbons.

Table 3. Comparison of reported strategies to ICE of HC anodes and the corresponding ICE gains (ΔICE, percentage points), against this work.

Precursor	Pyrolysis temp (℃)	Regulation strategy	Electrolyte	ICE before (%)	ICE after (%)	Δ ICE (%)	ref.
locust wood	1000-1500	Temp. optimization (acid-treated vs untreated)	1 M $NaClO_4$ in EC/DMC (1:1, v/v)	62.0	67.0	+5.0	38
Camphor wood	1300	Heating-rate control (optimized at 0.25 ℃/min)	1 M $NaClO_4$ in EC/DMC (1:1, v/v)	60.8	82.8	+22.0	39
Paulownia xylem	1000-1400	Temp. optimization	1 M $NaPF_6$ in diglyme	76.8	85.9	+9.1	40
Sucrose	1000-1600	Coating +Temp. optimization	1 M $NaClO_4$ in EC/DMC (1:1, v/v)	54.0	83.0	+29	41
Commercial HC	N/A	electrolyte selection	TEGDME and carbonate-based electrolytes	64.6	70.3	+5.7	42
Soy protein	800	Heteroatom doping + electrolyte selection	$NaPF_6$ and $NaCF_3SO_3$ in diglyme	44.2	62.1	+17.9	43
Commercial HC	N/A	Pre-sodiation	1 M $NaClO_4$ in PC/EC/DMC (1:1:1, v/v/v)	50.0	95.0	+45.0	44
Waste-wood	900	Catalytic graphitization+ electrolyte selection	10 mol% NaFSI–EMIFSI; 50:50 mol% NaFSI–C_3mpyrFSI; 1 M $NaPF_6$ in EC/PC (1:1, v/v)	26.0	41.0	+15.0	**This study**
Waste-wood	900	pre-sodiation	10 mol% NaFSI–EMIFSI	41.0	75.0	+34.0	**This study**

View Article Online
DOI: 10.1039/D6MA00412A

Conclusion

This study demonstrates a practical route to reduce first-cycle losses in wood-waste hard carbon by combining microstructure control, electrolyte selection, and pre-sodiation. MOF-assisted catalytic processing improved carbon ordering and delivered the best first-cycle performance among the tested catalysts, increasing ICE from 26% (WW) to 41.5% with a first-charge capacity of 191 mAh g^{-1}.

Electrolyte chemistry also affected both the first cycle and longer-term cycling. Although 1 M $NaPF_6$ in EC/PC gave a slightly higher ICE (42%), the FSI-based ionic-liquid electrolytes delivered higher reversible capacities (up to 195 mAh g^{-1}) and better capacity retention. Among them, NaFSI–C_3MPYRFSI (50:50 mol%) provided the highest capacity and the most stable cycling under the tested conditions. Pre-sodiation was also effective: an optimized contact time increased ICE to 75%, while longer contact reduced reversible capacity, highlighting the need to control the pre-sodiation level.

Beyond first-cycle efficiency, the Fe-MOF-treated carbon showed improved kinetics and durability: impedance after formation was reduced, rate capability was enhanced across the tested current range, and stable cycling was maintained for 200 cycles with coulombic efficiency approaching ~100% after formation. Overall, these results provide clear guidance on improving ICE in sustainable hard carbon anodes without compromising rate performance or long-term stability.

CRediT authorship contribution statement:

Sherif Hegazy: Conceptualization, Methodology, Formal analysis, Investigation, Data analysis and Writing – original draft. **Nolene Byrne:** Conceptualization, Methodology, Investigation, Resources, and Writing - Review & Editing, **Ahmed Abdelrahim:** Formal analysis. **Tao Hu:** Formal analysis, **Varsha Srivastava:** Supervision, **Sari Tuomikoski:** Supervision, **Ulla Lassi:** Supervision, Writing - Review & Editing, Resources, Project administration, Funding acquisition.

Conflicts of Interest

The authors declare no conflict of interest.

View Article Online
DOI: 10.1039/D6MA00412A

Data Availability Statement

Data will be stored in CSC´s Fairdata IDA repository and it will be found at Etsin (https://etsin.fairdata.fi/) after acceptance.

Acknowledgments

The first author acknowledges the support and facilities provided by the Battery Hub at Deakin University and thank the team for their guidance and assistance during the experimental work. Financial support from the BlackGreen project (Project No. 2430480911), co-funded by the European Regional Development Fund (ERDF) and the European Union, is gratefully acknowledged. Sherif Hegazy also acknowledges personal grant support from the Alfred Kordelin Foundation. Special thanks are extended to Dr. Ali Huerta, Ms. Riikka Koski, and Mr. Tommi Kokkonen for their dedicated efforts and valuable contributions to this work.

View Article Online
DOI: 10.1039/D6MA00412A

References

1 A. Nekahi, M. R. Anil Kumar, S. Deng, X. Li, A. Petropoulos, J. Nanda and K. Zaghib, *Electrochemical Energy Reviews*, DOI:10.1007/s41918-025-00247-y.

2 Y. Gao, Q. Yu, H. Yang, J. Zhang and W. Wang, *Advanced Materials*, DOI:10.1002/adma.202405989.

3 B. Zhong, C. Liu, D. Xiong, J. Cai, J. Li, D. Li, Z. Cao, B. Song, W. Deng, H. Peng, H. Hou, G. Zou and X. Ji, *ACS Nano*, 2024, **18**, 16468–16488.

4 Y. Yang, C. Wu, X. X. He, J. Zhao, Z. Yang, L. Li, X. Wu, L. Li and S. L. Chou, *Adv. Funct. Mater.*, DOI:10.1002/adfm.202302277.

5 W. Wang, B. Wang, Y. Li, N. Wang, Y. Xu, C. Wang, Y. Sun and H. Hu, *Chem. Asian J.*, DOI:10.1002/asia.202301146.

6 X. X. He, L. Li, X. Wu and S. L. Chou, *Advanced Materials*, DOI:10.1002/adma.202506066.

7 B. Yang, J. Wang, Y. Zhu, K. Ji, C. Wang, D. Ruan and Y. Xia, *J. Power Sources*, DOI:10.1016/j.jpowsour.2021.229656.

8 M. Zhang, Y. Li, F. Wu, Y. Bai and C. Wu, *Nano Energy*, DOI:10.1016/j.nanoen.2020.105738.

9 Z. Li, Y. Chen, Z. Jian, H. Jiang, J. J. Razink, W. F. Stickle, J. C. Neuefeind and X. Ji, *Chemistry of Materials*, DOI:10.1021/acs.chemmater.8b00645.

10 Y. Fang, M. Lu, H. Qian, J. Xiang, F. Tu, Y. Jiang, Y. Gan, X. He, H. Huang, X. Xia, Y. Xia, W. Zhang and J. Zhang, *ACS Appl. Energy Mater.*, DOI:10.1021/acsaem.5c00828.

11 J. Liu, B. Sun, Y. Xu, J. Wang, S. Liang, J. Wang, J. Zhang, Z. Yang, H. Yang, J. Yang, W. Li and X. Li, *Small*, DOI:10.1002/smll.202504810.

12 W. Shao, H. Shi, X. Jian, Z. S. Wu and F. Hu, *Advanced Energy and Sustainability Research*, DOI:10.1002/aesr.202200009.

13 R. Yuan, H. Wang, L. Shang, R. Hou, Y. Dong, Y. Li, S. Zhang, X. Chen and H. Song, *ACS Appl. Mater. Interfaces*, DOI:10.1021/ACSAMI.2C19798.

14 L. Habib, G. Suo, N. Habib, M. Aqdas, C. Lin, J. Li and S. Javed, *J. Energy Storage*, DOI:10.1016/j.est.2025.118821.

15 J. Li, G. Suo, C. Lin, J. Li, X. Luo, G. Yang, L. Habib, Z. K. Kalkozova and K. Naseem, *Chemical Engineering Journal*, DOI:10.1016/j.cej.2026.173031.

16 C. Lin, G. Suo, R. Mu, B. Zhao, J. Li, X. Hou, X. Ye, Y. Yang and L. Zhang, *J. Power Sources*, DOI:10.1016/j.jpowsour.2024.235426.

17 J. Cui, P. Su, W. Li, X. Wang, Y. Zhang, Z. Xiao, Q. An and Z. Chen, *Adv. Energy Mater.*, DOI:10.1002/aenm.202404604.

18 S. Hegazy, A. Ghannami, G. S. dos Reis, T. Hu, R. Brahmi, S. Tuomikoski, U. Lassi and V. Srivastava, *Chem. Eng. Sci.*, DOI:10.1016/j.ces.2024.120785.

19 S. Hegazy, K. Saaranen, T. Hu, S. Tuomikoski, U. Lassi and V. Srivastava, *RSC Adv.*, DOI:10.1039/d5ra04089b.

20 C. D. M. Saavedra Rios, L. Simonin, A. De Geyer, C. M. Ghimbeu and C. Dupont, *Energies (Basel).*, DOI:10.3390/en13143513.

21 A. Gomez-Martin, J. Martinez-Fernandez, M. Ruttert, M. Winter, T. Placke and J. Ramirez-Rico, *Chemistry of Materials*, DOI:10.1021/acs.chemmater.9b01768.

22 J. Conder, C. Villevieille, J. M. Le Meins and C. M. Ghimbeu, *ACS Appl. Energy Mater.*, DOI:10.1021/acsaem.2c01984.

23 S. Hegazy, C. M. Subramaniyam, A. Abdelrahim, R. Sliz, T. Hu, S. Tuomikoski, U. Lassi, F. García-Alvarado and V. Srivastava, *ChemElectroChem*, DOI:10.1002/celc.202500195.

24 S. Hegazy, A. Abdelrahim, R. Sliz, T. Hu, S. Tuomikoski, V. Srivastava and U. Lassi, DOI:10.1016/j.biombioe.2026.109142.

25 C. M. Subramaniyam, N. R. Srinivasan, Z. Tai, H. K. Liu and S. X. Dou, *RSC Adv.*, DOI:10.1039/c6ra27836a.

26 A. Ponrouch, E. Marchante, M. Courty, J. M. Tarascon and M. R. Palacín, *Energy Environ. Sci.*, DOI:10.1039/c2ee22258b.

27 K. Hankins, M. H. Putra, J. Wagner-Henke, A. Groß and U. Krewer, *Adv. Energy Mater.*, DOI:10.1002/aenm.202401153.

28 S. A. Ferdousi, L. A. O'Dell, M. Hilder, A. J. Barlow, M. Armand, M. Forsyth and P. C. Howlett, *ACS Appl. Mater. Interfaces*, DOI:10.1021/acsami.0c18119.

29 S. A. Ferdousi, L. A. O'Dell, J. Sun, Y. Hora, M. Forsyth and P. C. Howlett, *ACS Appl. Mater. Interfaces*, DOI:10.1021/acsami.1c24812.

30 F. Makhlooghiazad, L. Huang, N. Byrne, P. C. Howlett and M. Forsyth, *Adv. Energy Mater.*, DOI:10.1002/aenm.202506236.

31 M. Bellusci, E. Simonetti, M. De Francesco and G. B. Appetecchi, *Applied Sciences (Switzerland)*, DOI:10.3390/APP10186323.

32 G. Maresca, A. Petrongari, S. Brutti and G. Battista Appetecchi, *ChemSusChem*, DOI:10.1002/cssc.202300840.

33 I. Moeez, H. G. Jung, H. D. Lim and K. Y. Chung, *ACS Appl. Mater. Interfaces*, DOI:10.1021/acsami.9b14381.

34 Y. Wang, Z. Yu, Q. Li and Y. Liu, *Chemical Communications*, DOI:10.1039/d5cc04339e.

35 H. R. Sarma, J. Sun, I. E. Gunathilaka, Y. Hora, M. Forsyth and N. Byrne, *Sustainable Materials and Technologies*, DOI:10.1016/j.susmat.2024.e00846.

36 X. Tang, F. Xie, Y. Lu, H. Mao, Z. Chen, H. Pan, S. Weng, Y. Yang, X. Li, Z. Guo, Q. Guo, F. Ding, X. Hou, Y. Li, X. Wang, M. M. Titirici, L. Chen, Y. Pan and Y. S. Hu, *ACS Energy Lett.*, DOI:10.1021/acsenergylett.4c00041.

37 A. Adamson, R. Väli, M. Paalo, J. Aruväli, M. Koppel, R. Palm, E. Härk, J. Nerut, T. Romann, E. Lust and A. Jänes, *RSC Adv.*, DOI:10.1039/d0ra03212c.

38 J. Huo, C. Li, P. Xia, N. Fan, W. Mao and K. Bao, *J. Appl. Electrochem.*, DOI:10.1007/s10800-024-02235-4.

39 S. Guo, Y. Chen, L. Tong, Y. Cao, H. Jiao, Z. long and X. Qiu, *Electrochim. Acta*, DOI:10.1016/j.electacta.2022.140017.

40 J. Xu, B. Chen, B. Hu, Y. Gu, X. Li, Y. Liu, D. Sha, J. Zhang and S. Huang, *J. Energy Storage*, DOI:10.1016/j.est.2023.110306.

41 Y. Li, S. Xu, X. Wu, J. Yu, Y. Wang, Y. S. Hu, H. Li, L. Chen and X. Huang, *J. Mater. Chem. A Mater.*, DOI:10.1039/c4ta05451b.

42 B. Xiao, F. A. Soto, M. Gu, K. S. Han, J. Song, H. Wang, M. H. Engelhard, V. Murugesan, K. T. Mueller, D. Reed, V. L. Sprenkle, P. B. Balbuena and X. Li, *Adv. Energy Mater.*, DOI:10.1002/aenm.201801441.

43 C. Chen, Y. Huang, M. Lu, J. Zhang and T. Li, *Carbon N. Y.*, DOI:10.1016/j.carbon.2021.07.040.

44 M. Liu, J. Zhang, S. Guo, B. Wang, Y. Shen, X. Ai, H. Yang and J. Qian, *ACS Appl. Mater. Interfaces*, DOI:10.1021/acsami.0c02230.

View Article Online
DOI: 10.1039/D6MA00412A

- The data supporting this article have been included as part of the Supplementary Information.
- Original research data will also be stored in CSC´s Fairdata IDA repository and it will be found at Etsin (https://etsin.fairdata.fi/) after acceptance.